

Transient, Biocompatible Electronics and Energy Harvesters Based on ZnO

Canan Dagdeviren, Suk-Won Hwang, Yewang Su, Stanley Kim, Huanyu Cheng, Onur Gur, Ryan Haney, Fiorenzo G. Omenetto, Yonggang Huang, and John A. Rogers*

Semiconducting oxides are of growing interest as replacements for silicon in thin film transistors for active matrix display backplanes; they are also of potential use in transparent, flexible electronics and energy harvesters. Zinc oxide (ZnO), in particular, has a favorable combination properties, including excellent transparency in the visible wavelength range,^[1] high electron mobility,^[2] and strong piezoelectric response.^[3] As a result, ZnO, in forms ranging from films to wires and rods, has been explored in sensing,^[4–6] catalysis,^[7,8] optical emission,^[9,10] piezoelectric transduction,^[11] and actuation.^[12] Previous work also suggests that ZnO is biocompatible,^[13–15] and therefore suitable for devices that integrate on or in the human body. Here we introduce classes of ZnO based electronic devices that have, as their key attribute, the ability to dissolve completely in water or biofluids. In this way, ZnO provides an alternative to silicon^[16] or organic semiconductors^[17–20] for physically transient forms of electronics

and sensors, with expanded capabilities in energy harvesting, light emission and others. The other constituent materials of the devices presented here include magnesium (Mg) for electrodes and interconnects, magnesium oxide (MgO) for the dielectrics, and films of silk fibroin for the substrate and package. Each material used here is also biocompatible, as discussed in previous reports.^[21,22,23–26] We present specific designs and fabrication schemes for ZnO thin film transistors and mechanical energy harvesters (also for use as strain gauges). Detailed studies reveal the kinetics of dissolution and the ability to use materials and design choices to control this kinetics. Combined experimental/theoretical work illustrates the key operational features of the devices.

Figure 1a and **b** provide a schematic diagram and an image of water-soluble ZnO thin film transistors (TFTs) and mechanical energy harvesters (MEHs)/ strain gauges. Sheets of silk fibroin provide substrates and, in certain cases,

C. Dagdeviren, S.-W. Hwang, S. Kim, R. Haney,
 Prof. J. A. Rogers
 Department of Materials Science and Engineering
 University of Illinois at Urbana-Champaign
 Urbana, Illinois 61801, USA
 E-mail: jrogers@illinois.edu

C. Dagdeviren, S.-W. Hwang, S. Kim, R. Haney, Prof. J. A. Rogers
 Frederick Seitz Materials Research Laboratory
 University of Illinois at Urbana-Champaign
 Urbana, Illinois 61801, USA

C. Dagdeviren, S.-W. Hwang, S. Kim, R. Haney, Prof. J. A. Rogers
 Beckman Institute for Advanced Science and Technology
 University of Illinois at Urbana-Champaign
 Urbana, Illinois 61801, USA

Y. Su, H. Cheng, Prof. Y. Huang
 Department of Mechanical Engineering
 Northwestern University
 Evanston, Illinois 60208, USA

Y. Su, H. Cheng, Prof. Y. Huang
 Department of Civil and Environmental Engineering
 Northwestern University
 Evanston, Illinois 60208, USA

Y. Su
 Center for Mechanics and Materials
 Tsinghua University
 Beijing 100084, China

DOI: 10.1002/sml.201300146

O. Gur, Prof. J. A. Rogers
 Department of Electrical and Computer Engineering
 University of Illinois at Urbana-Champaign
 Urbana, Illinois 61801, USA

O. Gur
 William L. Everitt Laboratory
 University of Illinois at Urbana-Champaign
 Urbana, Illinois 61801, USA

F. G. Omenetto
 Department of Biomedical Engineering
 Tufts University
 Medford, Massachusetts 02155, USA

F. G. Omenetto
 Department of Physics
 Tufts University
 Medford, Massachusetts 02155, USA

Prof. J. A. Rogers
 Department of Chemistry
 University of Illinois at Urbana-Champaign
 Urbana, Illinois 61801, USA

Prof. J. A. Rogers
 Department of Mechanical Science and Engineering
 University of Illinois at Urbana-Champaign
 Urbana, Illinois 61801, USA



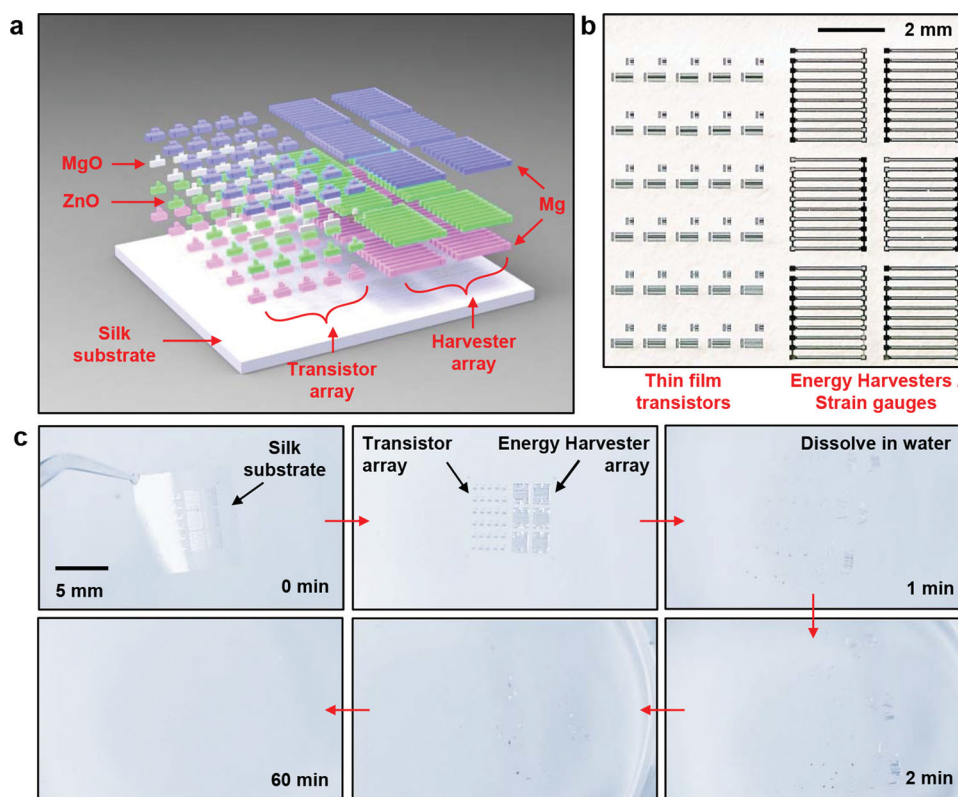


Figure 1. Materials and designs for transient thin film transistors (TFTs) and mechanical energy harvesters (MEHs)/strain gauges based on ZnO, Mg, MgO, and silk. a) Schematic illustration of transient ZnO TFTs and MEHs/strain gauges that consist entirely of water soluble materials: ZnO (semiconductor/piezoelectric), Mg (conductor), MgO (insulator), silk (substrate). b) Photograph of a collection of ZnO TFTs and MEHs on a silk substrate. All electronic materials were deposited through high-resolution shadow masks made of polyimide (PI) film (Kapton, 12.5 μm , Dupont, USA). c) A set of images of an array of ZnO TFTs and MEHs on silk, at various times after immersion in deionized water at room temperature.

encapsulating layers. Magnesium, deposited by electron beam evaporation through fine-line stencil masks made of polyimide (PI) films (Kapton, 12.5 μm , Dupont, USA), is used for the electrodes and interconnects (thicknesses between 200 and 500 nm). A first layer of Mg defines the source/drain electrodes for the TFTs (and, therefore the channel length, L_{ch}) and the bottom electrodes of the MEHs. Sputter deposition of thin films of ZnO (thicknesses between 350 and 500 nm) through PI masks forms semiconducting and piezoelectric components of the devices. The widths of the patterned ZnO films determine the channel widths (W) of the transistors. Layers of MgO (thicknesses between 100 and 150 nm) deposited by electron beam evaporation through PI masks serve as the gate dielectric layers for the TFTs. An additional patterned deposition of Mg (~ 400 nm) yields top electrodes for MEHs, and source, drain and gate contacts for the TFTs. A top encapsulating layer of silk can be applied by spin casting. All constituent materials, i.e. Mg (electrodes, contacts and interconnects), MgO (gate and interlayer dielectrics), ZnO (active material for the TFTs and energy harvesters/ strain gauges) and silk (substrate and encapsulant), dissolve in water. The products of this dissolution include $\text{Mg}(\text{OH})_2$, $\text{Si}(\text{OH})_4$ and $\text{Zn}(\text{OH})_2$. Previous studies suggest that these compounds, and the device materials themselves, are biocompatible and environmentally benign.^[14,27,28] Figure 1c includes a set of images collected in a time sequence during dissolution in deionized

water (DI) at room temperature. The silk substrate (~ 25 μm), in the formulation used for this example, quickly disappears by simple dissolution. This process causes the device structures to physically disintegrate. Afterward, each remaining material disappears due to hydrolysis at different rates, as described in the following sections and previous reports.^[29–33] The time frames for dissolution can be programmed not only by encapsulation and packaging methods, but also by choices of dimensions, thicknesses and configurations in the materials for the device structures.

Dissolution of the constituent materials, other than the silk, involves hydrolysis to produce metal hydroxides. In the case of ZnO, the product is zinc hydroxide ($\text{Zn}(\text{OH})_2$), as a result of the reaction $\text{ZnO} + \text{H}_2\text{O} \leftrightarrow \text{Zn}(\text{OH})_2$. Figure 2a shows a collection of images of a meander trace of ZnO (200 nm) at various times during hydrolysis. The trace completely disappears after 15 hours, in DI water at room temperature. The mechanisms of dissolution of ZnO can be analytically described by reactive diffusion models, in which water diffusion into the materials is the rate limiting process. Previous reports describe in detail the dissolution behaviors of ZnO and the dependence on pH, temperature, dimensions and surface structures.^[27,34–37] Additional experiments on dissolution, monitored by measurements of thickness as a function of time during immersion in several different types of solutions, such as phosphate buffer saline (PBS, pH 4.0, Sigma-

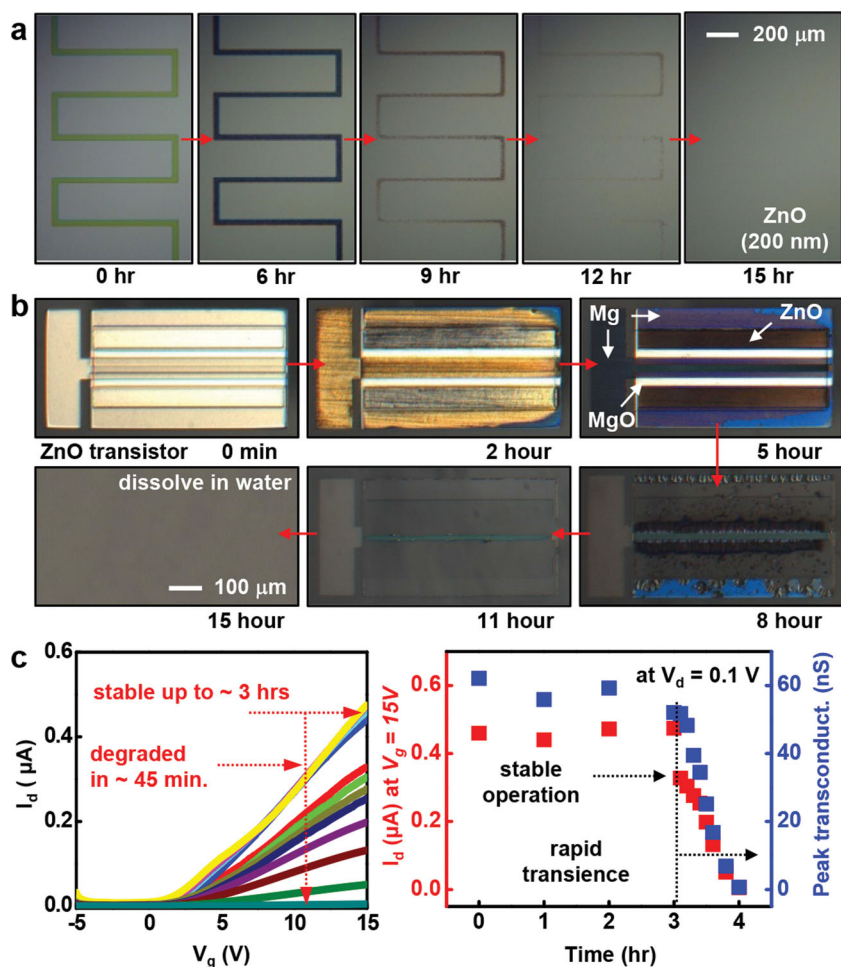


Figure 2. Dissolution kinetics of water soluble electronic materials, and devices. a) A series of optical microscope images collected at various times during dissolution of a meander trace of ZnO (200 nm) immersed in deionized water at room temperature. b) Images of a representative ZnO TFT at various times during dissolution. All components fully dissolve. c) Experimental results of degradation in electrical properties of a ZnO TFT encapsulated with MgO (500 nm) at various times after immersion in DI water. The linear scale transfer curves (left) and the drain current (I_d) at drain and gate voltages of $V_d = 0.1\text{V}$ and $V_g = 5\text{V}$, respectively, and the peak transconductance (left) show that the operation of the device is stable for ~3 h, after which the properties quickly degrade in ~45 min.

Aldrich, USA) serum, and comparison of the results with theoretical models (see SI for details) appear in Figure S1a. The rate of dissolution ZnO increases with decreasing pH, consistent with a previous literature report.^[27] In acidic solution, the dissolution of ZnO is also attributed to the reaction, $\text{ZnO} + 2\text{H}^+ \rightarrow \text{Zn}_2 + \text{H}_2$. A set of optical micrographs shows a fully formed ZnO TFT undergoing dissolution under similar conditions, as presented in Figure 2b. All electronic materials, i.e. Mg, MgO and ZnO, completely dissolve in 15 h after immersion in DI water at room temperature, in a controlled manner, without cracking, flaking or delamination. For the device dimensions studied here, the thicknesses of the layers determine, in large part, the timescales for dissolution.

Figure 2c summarizes the temporal variation in the electrical properties of a ZnO TFT, as it dissolves. (See Figure S1b for an image and diagram of the device.) In this case, a plate of glass serves as the substrate, and a layer of MgO (500 nm), deposited by electron beam evaporation, encapsulates

the entire system everywhere except at the contacts for source, drain, and gate electrodes which themselves are not immersed. Measured transfer curves, drain currents (I_d) and peak transconductances show stable operation for ~3 h, followed by rapid degradation over the next ~45 min. (Additional electrical properties appear in Figure S1c.) The encapsulant and the device materials (mainly the Mg in this case) define the first and second timescales, respectively. The results of Figure 2c are only representative. The encapsulant material and thickness can be selected to achieve stable periods of device operation that match requirements for specific applications. For example, silk can be combined with MgO to enable the lifetime to extend from minutes to years, as demonstrated in a previous result.^[16] Complete electrical and mechanical characterization of ZnO TFTs and MEHs appear in Figure 3. All electrical measurements and bending studies were performed in a dry environment. Here, the TFTs use Mg (150 nm, source, drain and gate electrodes), ZnO (200 nm, active layer), MgO (100 nm, gate dielectric). Figure 3b illustrates additional details in optical micrographs of a typical TFT, collected after defining the channel configuration (top) and completing the fabrication (bottom). Analysis of current-voltage (I - V) characteristics (Figure 3c,d) of a typical device (channel length (L_{ch}) and width (W) are 20 μm and 500 μm , respectively) yields a mobility of $\sim 0.95\text{ cm}^2/\text{V}\cdot\text{s}$, an on/off ratio of $>10^3$, a subthreshold swing of $\sim 1\text{ V}/\text{dec}$ (at $V_d = 0.1\text{ V}$) and a threshold voltage of $\sim 1\text{ V}$. (See details on contact resistance of Mg

in Figure S1d). These properties are similar to those of non-transient counterparts.^[38–41] Previous literature studies suggest that deposition procedures and subsequent processing conditions for ZnO strongly affect the electrical properties.^[38,42–45] Careful parametric studies reveal conditions for sputter deposition that yield transistor characteristics (i.e. mobilities, on/off ratios, etc) in transient devices on silk that fall into a well established range set by more conventional sets of materials and substrates.^[40,46]

Figure 3e presents an image of an array of MEHs, each with a capacitor type geometry. A layer of ZnO (500 nm) lies between bottom (300 nm) and top electrodes (500 nm) of Mg that define an active area of 50 $\mu\text{m} \times 2\text{ mm}$. An MEH consists of six groups of devices; each group includes ten separate capacitor structures electrically connected in parallel. The six groups are connected in series. A IPC Flexural Endurance Tester (Model: CK-700FET) enables accurate evaluation of properties under bending. The test configuration involves the

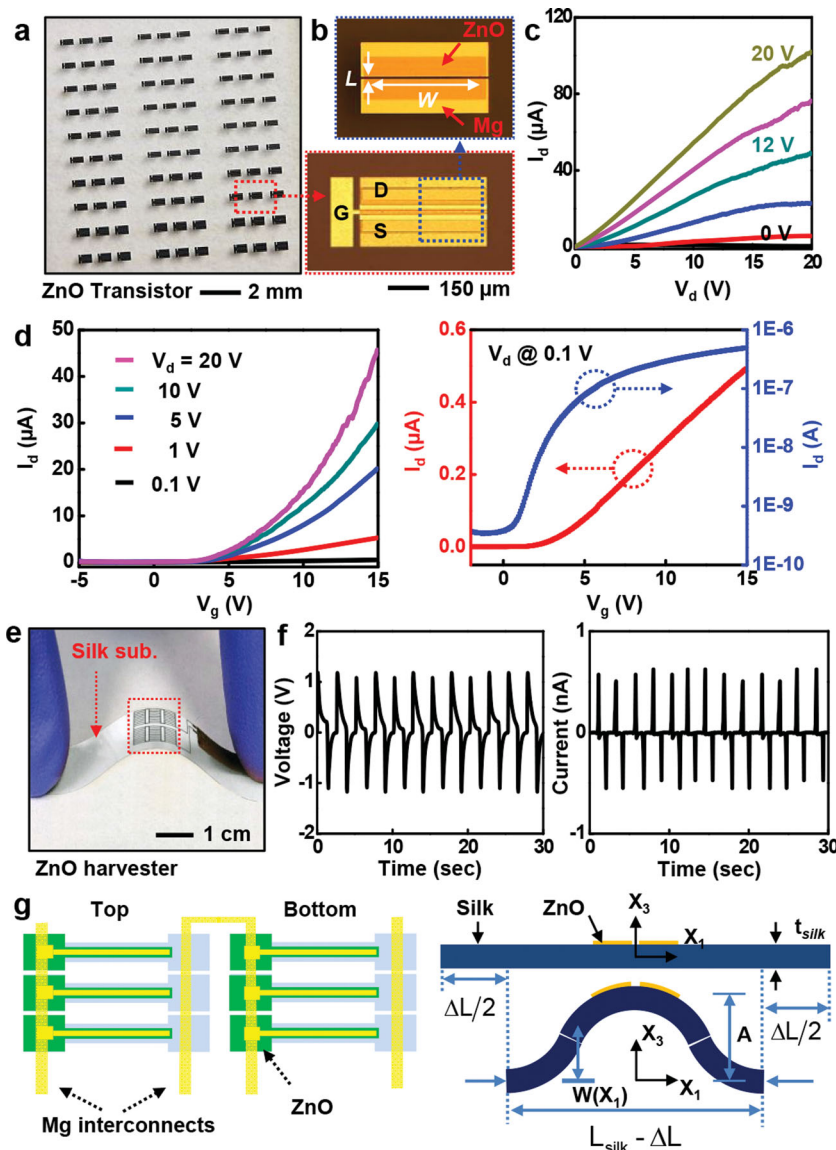


Figure 3. Electrical characterization of ZnO TFTs and MEHs. a) Image of an array of ZnO TFTs on a silk substrate. The devices use Mg (source, drain, and gate electrodes), ZnO (active layer) and MgO (gate dielectric). b) Optical micrographs of a TFT, after defining the channel configuration (top), and after completing the fabrication (bottom). c) Current-voltage characteristics of a typical device, at different gate biases. d) Linear scale transfer curves at various drain voltages (left), and linear (red) and log scale (blue) transfer curves at a drain voltage of 0.1 V (right). e) Optical micrograph of a transient, ZnO energy harvester on a thin film silk substrate, in a bent configuration. f) Output voltage vs time and output current vs time during cycles of bending. g) Schematic illustration of ZnO strips connected in series, and the theoretical shape for buckling of a device under compression.

two edges of the sample fixed within the two sliding fixtures of the instrument. During compression, the sample mechanically buckles upward to generate a well-defined, although non-uniform bending moment. Periodic variations in positive and negative voltage output peaks accompany the application and release of the buckling stresses (tensile at the location of the devices), respectively. The voltage and current outputs from an MEH are ~ 1.14 V and ~ 0.55 nA, as shown in Figure 3f. The peak output power density is ~ 10 nW/cm². The output averaged over the entire range of deformation, combined with a theoretical analysis of the mechanical input

power required to bend the device, suggests a conversion efficiency of 0.28%, but in a way that is dependent on many parameters of the system, including the external electrical load. See Supporting Information. The structures are not fully optimized for efficiency. High absolute efficiencies might not be a relevant goal for many applications in bio-integrated devices. In such cases, the aim is to collect enough power to operate a device (e.g. a pacemaker), but to do so without inducing significant mechanical loading on natural motions of the relevant part of the body. High efficiency operation would, necessarily, impose constraints on motion, due to conversion of a significant fraction of mechanical work into electrical power. Such constraints can have adverse biological consequences, particularly in an organ like the heart which responds to mechanical loading by arrhythmic behavior. The efficiency can be improved through optimized choices of thicknesses, lengths, widths and Young's moduli for the substrate and piezoelectric layers.^[47] Furthermore, reduction in viscoelastic dissipation of the substrate can be beneficial.^[42] Figure 3g gives a schematic illustration of narrow strips of ZnO films connected in series, and the theoretically predicted shape of the buckled device.

Analytical models that couple the mechanical deformation and the piezoelectric effect provide additional insights into the behaviours. Compression of the silk substrate of length L_{silk} leads to its buckling with a representative out-of-plane displacement $w = A[1 + \cos(2\pi x_1/L_{silk})]/2$, where the origin of coordinate x_1 is at the center of silk substrate, and the amplitude A is related to the compression ΔL between two ends of the silk substrate by $A \approx (2/\pi)\sqrt{L_{silk} \cdot \Delta L}$ (see SI for details). The ZnO strips, together with the top and bottom electrodes, bend with the buckled silk substrate. The strain in the ZnO consists of membrane and bending strains. The membrane strain is given analytically by $\varepsilon_m = 4\pi\sqrt{\Delta L/L_{silk}}(\overline{E}I_{silk}/\overline{E}I_{comp})(h/L_{silk})$ ^[48] (see SI for details), where $\overline{E}I_{silk}$ and $\overline{E}I_{comp}$ are the bending stiffnesses of the silk substrate and the composite structure of ZnO strips with electrodes and silk substrate, respectively; and h is the distance between the center of ZnO strips and the neutral mechanical plane of the composite structure (Figure S2). The bending strain is much smaller than the membrane strain since the ZnO strips are very thin. As a result, the total strain is essentially the same with the membrane strain. In addition, the bending strain has opposite signs above and below the center

of ZnO strips and does not contribute to the voltage and current output of the MEH (see SI for details).

The ZnO strips are transversely isotropic with elastic, piezoelectric, and dielectric constants c_{ij} , e_{ij} , and k_{ij} , respectively. The polarization direction x_3 is normal to the surface of the strip and the surface of the silk substrate. For plane-strain deformation ($\epsilon_{22} = 0$) the strain ϵ_{33} and the electric field E_3 along the polarization direction x_3 satisfy the constitutive relations $0 = c_{13}\epsilon_{11} + c_{33}\epsilon_{33} - e_{31}E_3$ and $D_3 = e_{31}\epsilon_{11} + e_{33}\epsilon_{33} + k_{33}E_3$, where the electric displacement D_3 along the polarization direction is a constant to be determined. For measurements of current, the top and bottom electrodes are connected to an ammeter as shown in Figure S2b. The ammeter has negligible electrical resistance, and therefore negligible voltage drop. The current (through the electrodes and ammeter) results from the moving charge induced by the strain in the ZnO (i.e., piezoelectric effect) even without voltage between the top and bottom electrodes. The zero voltage between the top and bottom electrodes of each ZnO strip, together with the above equations, gives $D_3 = \bar{e}\epsilon_m$ $\bar{e} = e_{31} - (c_{13}/c_{33})e_{33}$, where \bar{e} is the effective piezoelectric constant. For each group of device in series, the current is given by $I = -A_{ZnO}D_3$, where A_{ZnO} is total area of ZnO strips in each group. For a representative compression $\Delta L = \Delta L_{\max}[1 - \cos(2\pi t/T)]^2/4$ with the maximum compression ΔL_{\max} and period T , the maximum current is obtained as

$$I_{\max} = 4\pi^2 \frac{(-\bar{e}) A_{ZnO}}{T} \frac{\bar{E}I_{\text{silk}}h}{\bar{E}I_{\text{comp}}L_{\text{silk}}} \sqrt{\frac{\Delta L_{\max}}{L_{\text{silk}}}} \quad (1)$$

For $\Delta L_{\max} = 1.5$ cm, $T = 2.3$ second and $L_{\text{silk}} = 3$ cm as in experiments, $\bar{E}I_{\text{silk}}/\bar{E}I_{\text{comp}} = 0.34$, $h = 5.5$ μm and $A_{ZnO} = 1.08$ mm^2 from the specimen geometry (see SI for details), and $\bar{e} = -0.67$ C/m², which is on the same order of magnitude as the literature values.^[8,49] Equation (1) gives the maximum current $I_{\max} = 0.55$ nA, which agrees well with the experimental result as shown in Figure 3f.

For measurements of voltage, if V denotes the total voltage for n groups of devices in series, then the voltage across each group is V/n . The electric displacement becomes $D_3 = \bar{e}\epsilon_m + \bar{k}V/(nt_{ZnO})$, where $\bar{k} = k_{33} + (e_{33}^2/c_{33})$ is the effective dielectric constant and t_{ZnO} is the thickness of ZnO strips. The current $I = -A_{ZnO}D_3$ is also related to the voltage V and resistance R of the voltmeter by $I = V/R$, which gives $V/R = -A_{ZnO}\dot{D}_3$, or equivalently

$$\frac{dV}{dt} + \frac{nt_{ZnO}}{A_{ZnO}R\bar{k}}V = -\frac{n\bar{e}t_{ZnO}}{\bar{k}}\frac{d\epsilon_m}{dt} \quad (2)$$

For $\Delta L = \Delta L_{\max}[1 - \cos(2\pi t/T)]^2/4$ and the initial condition $V(t=0) = 0$, the maximum voltage is given by

$$V_{\max} \approx 4\pi^2 R \frac{(-\bar{e}) A_{ZnO}}{T} \frac{\bar{E}I_{\text{silk}}h}{\bar{E}I_{\text{comp}}L_{\text{silk}}} \sqrt{\frac{\Delta L_{\max}}{L_{\text{silk}}}} \quad (3)$$

For $R = 2.3 \times 10^9$ Ω in the experiment, the theory gives the maximum voltage 1.1V, which agrees well with experiment result of 1.14V. In addition to electrical characterization of devices, the intrinsic piezoelectric and morphological properties of active layer ZnO thin film by sputtering system

was studied by AFM, SEM, and XRD techniques in detail (Figure S3).

The results presented here indicate that ZnO can be used effectively as an active material for transient electronics, as well as for energy harvesting and strain sensing devices, for which all of the constituent elements dissolve completely in water. Compared to silicon, ZnO has features, such as wide, direct bandgap and piezoelectric responses, that could enable expanded capabilities in transient devices. The use of this material alone, or in heterogeneous configurations with silicon, opens up additional application possibilities for transient technologies, in areas ranging from biomedicine, to environmental monitoring and certain areas of consumer electronics.

Experimental Section

Fabrication of ZnO TFTs and MEHs: All electronic materials were directly deposited onto silk substrates through high resolution stencil masks made of polyimide (PI) films (Kapton, 12.5 μm , Dupont, USA). These materials consist of ZnO (semiconductor), Mg (conductors), MgO (insulators), and silk (substrate). A layer of Mg (150 nm) deposited by electron beam evaporation (Temescal) defined the source and drain electrodes for the TFTs. ZnO (200 nm) deposited by RF magnetron sputtering (AJA) through a PI mask served as the semiconductor. A high-purity of ZnO target was used (99.99%), with base pressures of 2×10^{-6} torr, and working pressures of 15 mTorr, maintained with a Ar (99.99%):O₂ = 2:1 (sccm) gas mixture. The sputtering was performed at room temperature (RT) with an RF power of 250 W, immediately after cleaning the target with Ar plasma for 5 min. The deposition rate was ~ 150 nm/h. Electron beam evaporation of MgO (100 nm), also through PI masks, defined the gate dielectrics. The gate electrode consisted of Mg (300 nm), deposited and patterned using schemes similar to those for the source and drain.

ZnO MEHs were designed in six groups, each of which contains ten separate devices (ZnO strips with Mg electrodes on top and bottom, in a capacitor type geometry). Devices within each group were connected in parallel; the six groups themselves were connected in series. The fabrication began with deposition of Mg (300 nm) by electron beam evaporation through a PI shadow mask, to form bottom electrodes. A layer of ZnO (400–500 nm) was then formed by RF sputtering, through a shadow mask aligned to the Mg bottom electrodes. Top electrodes of Mg (~ 500 nm) were formed in a manner similar to that for the bottom electrodes. Individual ZnO strips defined active areas of $50 \mu\text{m} \times 2$ mm. Square pads at their ends facilitated electrical top and bottom contacts. The ZnO layer was formed in a geometry slightly bigger than that of the bottom electrode to avoid shorting of top to bottom, as seen in Figure S2.

Investigation of ZnO Thin-Film Properties and Device Analysis: X-ray diffraction (XRD, Philips X'pert) revealed that the films consist of hexagonal ZnO, with preferred orientation of (002). Scanning electron microscope (SEM, Hitachi S4800) imaging determined the surface topography and provided cross sectional views of the films. Measurements of voltage induced displacements in thin films of ZnO were conducted by atomic force microscopy (AFM, Asylum Cypher, USA). A semiconductor parameter analyzer (4155C, Agilent) was used to measure the electrical characteristics of TFTs and MEHs.

Bending Tests for Energy Harvesters/Strain Gauges: A commercial instrument (IPC Flexural Endurance Tester Model: CK-700FET) was used to perform bending experiments. The test involved compressing a sheet of devices between two clamped edges; the result was a buckling structure whose curvature was defined by the extent of compression. Electrical measurements revealed positive and negative swings in voltage and current output, corresponding to the application and release of such buckling stresses. An analytical model of the mechanical deformations and the associated piezoelectric effects captured the experimental observations.

Dissolution Experiments: Dissolution tests were performed to study degradation behaviors of devices and kinetics of materials removal. To observe dissolution of ZnO, a meander trace of ZnO (200 nm) on a glass substrate was submerged in DI water at room temperature. Optically significant changes were observed after 9 hours, and complete disappearance occurred in 15 h. In a similar way, a ZnO transistor, consisting of Mg, MgO, and ZnO, on glass was used to illustrate the various stages of dissolution at the device level. Most components disappeared within 8 h; complete dissolution occurred within 15 h. In addition, measurements of changes in electrical properties defined timescales of device function. A transistor with a design similar to that described above was prepared and encapsulated with a layer of MgO (500 nm). Measured and calculated characteristics revealed two-stage kinetics. The first was determined by the encapsulation layer; the second, primarily by the Mg electrodes.

Supporting Information

Supporting Information is available from the Wiley Online Library or from the author.

Acknowledgements

C. Dagdeviren and S.-W. Hwang contributed equally to this work. This material is based upon work supported by the Defense Advanced Research Projects Agency. Anoop Damodaran is acknowledged for support during PFM test.

- [1] S. Mondal, K. P. Kanta, P. Mitra, *J. Phys. Sci.* **2008**, *12*, 221.
- [2] K. Miyamoto, M. Sano, H. Kato, T. Yao, *J. Cryst. Growth* **2004**, *265*, 34.
- [3] M. H. Zhao, Z. L. Wang, S. X. Mao, *Nano Lett.* **2004**, *4*, 587.
- [4] S. K. Gupta, A. Joshi, M. Kaur, *J. Chem. Sci.* **2010**, *122*, 57.
- [5] N. Kumar, A. Dorfman, J. I. Hahm, *Nanotechnology* **2006**, *17*, 2875.
- [6] H. Gullapalli, V. S. M. Vemuru, A. Kumar, A. Botello-Mendez, R. Vajtai, M. Terrones, S. Nagarajiah, P. M. Ajayan, *Small* **2010**, *6*, 1641.
- [7] L. Saad, M. Riad, *J. Serb. Chem. Soc.* **2008**, *73*, 997.
- [8] B. V. Kumar, H. S. B. Naik, D. Girija, B. V. Kumar, *J. Chem. Sci.* **2011**, *123*, 615.
- [9] S. Baskoutas, G. Bester, *J. Phys. Chem. C* **2011**, *115*, 15862.
- [10] C. Czekała, J. Guinard, C. Hanisch, B. Q. Cao, E. M. Kaidashev, N. Boukos, A. Travlos, J. Renard, B. Gayral, D. L. S. Dang, M. Lorenz, M. Grundmann, *Nanotechnology* **2008**, *19*, 115202.
- [11] H. Choi-Yim, R. Busch, W. L. Johnson, *J. Appl. Phys.* **1998**, *83*, 7993.
- [12] F. R. Blom, D. J. Yntema, F. C. M. Van De Pol, M. Elwenspoek, J. H. J. Fluitman, T. J. A. Popma, *Sens. Actuat.* **1990**, *21*, 226.
- [13] Z. Li, R. Yang, M. Yu, F. Bai, C. Li, Z. L. Wang, *J. Phys. Chem. C* **2008**, *112*, 20114.
- [14] Y. F. Zheng, R. Z. Li, Y. D. Wang, *Int. J. Modern Phys. B* **2009**, *23*, 1566.
- [15] S. Dutta, S. Basak, P. K. Samanta, *Int. J. Nanosci. Nanotechnol.* **2012**, *3*, 27.
- [16] S. W. Hwang, H. Tao, D. H. Kim, H. Cheng, J. K. Song, E. Rill, M. A. Brenckle, B. Panilaitis, S. M. Won, Y. S. Kim, Y. M. Song, K. J. Yu, A. Ameen, R. Li, Y. Su, M. Yang, D. L. Kaplan, M. R. Zakin, M. J. Slepian, Y. Huang, F. G. Omenetto, J. A. Rogers, *Science* **2012**, *337*, 1640.
- [17] C. Legnani, C. Vilani, V. L. Calil, H. S. Barud, W. G. Quirino, C. A. Achete, S. J. L. Ribeiro, M. Cremona, *Thin Solid Films* **2008**, *517*, 1016.
- [18] M. Irimia-Vladu, P. A. Troshi, M. Reisinger, L. Shmygleva, Y. Kanbur, G. Schwabegger, M. Bodea, R. Schwödiauer, A. Mumyatov, J. W. Fergus, V. F. Razumov, H. Sitter, N. S. Sariciftci, S. Bauer, *Adv. Funct. Mater.* **2010**, *20*, 4069.
- [19] C. J. Bettinger, Z. Bao, *Polym. Int.* **2010**, *59*, 563.
- [20] C. J. Bettinger, Z. Bao, *Adv. Mater.* **2010**, *22*, 651.
- [21] B. Panilaitis, G. H. Altman, J. Chen, H. J. Jin, V. Karageorgiou, D. L. Kaplan, *Biomaterials* **2003**, *24*, 3079.
- [22] M. Moravej, D. Mantovani, *Int. J. Mol. Sci.* **2011**, *12*, 4250.
- [23] S. P. Hudson, R. F. Padera, R. Langer, D. S. Kohane, *Biomaterials* **2008**, *29*, 4045.
- [24] B. G. Trewyn, J. A. Nieweg, Y. Zhao, V. S. Y. Lin, *Chem. Engin. J.* **2008**, *137*, 23.
- [25] S. Shen, P. S. Chow, F. Chen, R. B. Tan, *Chem. Pharm. Bull.* **2007**, *55*, 985.
- [26] C. Martinez-Boubeta, L. Balcells, R. Cristòfol, C. Sanfeliu, E. Rodríguez, R. Weissleder, S. Lope-Piedrafita, K. Simeonidis, M. Angelakeris, F. Sandiumenge, A. Calleja, L. Casas, C. Monty, B. Martínez, *Nanomed. Nanotechnol. Biol. Med.* **2010**, *6*, 362.
- [27] J. Zhou, N. Xu, Z. L. Wang, *Adv. Mater.* **2006**, *18*, 2432.
- [28] I. Shimizu, D. MacFarlane, *Dermatol. Surgery* **2012**, *38*, 965.
- [29] M. H. Grosjean, L. Roué, *J. Alloys Compounds* **2006**, *416*, 296.
- [30] D. J. Wales, J. P. K. Doye, *J. Chem. Phys.* **2003**, *119*, 12409.
- [31] K. Wegner, H. C. Lya, R. J. Weissa, S. E. Pratsinisa, A. Steinfeldt, *Int. J. Hydrogen Energy* **2006**, *31*, 55.
- [32] R. B. Reed, D. A. Ladner, C. P. Higgins, P. Westerhoff, J. F. Ranville, *Environ. Toxicol. Chem.* **2012**, *31*, 93.
- [33] G. Song, A. Atrens, *Adv. Engin. Mater.* **2003**, *5*, 837.
- [34] M. Valtiner, S. Borodin, G. Grundmeier, *Langmuir* **2008**, *24*, 5350.
- [35] C. David, J. Galceran, C. Rey-Castro, J. Puy, E. Companys, J. Salvador, J. Monne, R. Wallace, A. Vakourov, *J. Phys. Chem.* **2012**, *116*, 11758.
- [36] H. Gerischer, N. Sorg, *Electrochim. Acta* **1992**, *37*, 827.
- [37] A. Mudunkotuwa, T. Rupasinghe, C. Wu, V. Grassian, *Langmuir* **2012**, *28*, 396.
- [38] H. Jeon, K. Noh, D. Kim, M. Jeon, *J. Korean Phys. Soc.* **2007**, *51*, 1999.
- [39] X. Zhang, J. Zhang, W. Zhang, X. Hou, *J. Mater. Sci. Mater. Electron.* **2010**, *21*, 671.
- [40] R. Hoffman, B. Norris, J. Wagera, *Appl. Phys. Lett.* **2003**, *82*, 733.
- [41] P. F. Carcia, R. S. McLean, M. H. Reilly, *Appl. Phys. Lett.* **2006**, *88*, 123509.
- [42] C. Chang, V. H. Tran, J. Wang, Y. K. Fuh, L. Lin, *Nano Lett.* **2010**, *10*, 726.
- [43] G. B. Stringfellow, *Organometallic Vapor-Phase Epitaxy: Theory and Practice*, Academic, San Diego **1998**, p.4.
- [44] S. Masuda, K. Kitamura, Y. Okumura, S. Miyatake, H. Tabata, T. Kawai, *J. Appl. Phys.* **2003**, *93*, 1624.

- [45] J. M. Camacho, R. Castro-Rodríguez, A. Iribarren, E. Chan y Díaz, A. Duarte-Moller, P. Sánchez Santiago, *Int. J. Phys. Sci.* **2011**, *6*, 6660.
- [46] C. J. Park, Y. W. Kim, Y. J. Cho, S. M. Bobade, D. K. Choi, S. B. Lee, *J. Korean Phys. Soc.* **2009**, *55*, 1925.
- [47] Q. M. Wang, X. H. Du, B. Xu, L. E. Cross, *Ultrasonics Ferroelec. Frequency Control. IEEE Trans.* **1999**, *46*, 638.
- [48] S.-I. Park, J.-H. Ahn, X. Feng, S. Wang, Y. Huang, J. A. Rogers, *Adv. Funct. Mater.* **2008**, *18*, 2673.
- [49] F. Bernardini, V. Fiorentini, D. Vanderbilt, *Phys. Rev. B* **1997**, *56*, 10024.

Received: January 15, 2013
Published online:

NANO MICRO
small

Supporting Information

for *Small*, DOI: 10.1002/smll.201300146

**Transient, Biocompatible Electronics and Energy Harvesters
Based on ZnO**

*Canan Dagdeviren, Suk-Won Hwang, Yewang Su, Stanley
Kim, Huanyu Cheng, Onur Gur, Ryan Haney, Fiorenzo G.
Omenetto, Yonggang Huang, and John A. Rogers**

Supporting Information for

Transient, Biocompatible Electronics and Energy Harvesters Based on ZnO

*Canan Dagdeviren, Suk-Won Hwang, Yewang Su, Stanley Kim, Huanyu Cheng, Onur Gur, Ryan Haney, Yonggang Huang, John A. Rogers**

[*] Prof. John A. Rogers Corresponding-Author
Department of Materials Science and Engineering, Chemistry, Mechanical Science and Engineering, Electrical and Computer Engineering
Beckman Institute for Advanced Science and Technology, and Frederick Seitz Materials Research Laboratory

University of Illinois at Urbana-Champaign

Urbana, Illinois 61801 (USA)

E-mail: jrogers@illinois.edu

Canan Dagdeviren, Suk-Won Hwang, Stanley Kim, Ryan Haney

Department of Materials Science and Engineering

Frederick Seitz Materials Research Laboratory

University of Illinois at Urbana-Champaign

Urbana, Illinois 61801 (USA)

Onur Gur

Department of Electrical and Computer Engineering

William L. Everitt Laboratory

University of Illinois at Urbana-Champaign,

Urbana, Illinois 61801 (USA)

Yewang Su

Department of Mechanical Engineering and Department of Civil and Environmental Engineering

Northwestern University

Evanston, Illinois 60208 (USA)

Center for Mechanics and Materials, Tsinghua University, Beijing 100084 (China)

Prof. Yonggang Huang, Huanyu Cheng

Department of Mechanical Engineering and Department of Civil and Environmental Engineering

Northwestern University

Evanston, Illinois 60208 (USA)

Keywords: Transient electronics, biocompatible electronics, zinc oxide, flexible electronics, mechanical energy harvesting

1. Dissolution of zinc oxide

To understand the dissolution mechanism of a ZnO film, the film thickness as a function of time in various solutions (e.g. PBS, DI water and bovine serum) was studied.

Upon dissolution, ZnO forms zinc hydroxide, following the equilibrium: $\text{ZnO} + \text{H}_2\text{O} \leftrightarrow$

$\text{Zn}(\text{OH})_2$.^[1] The initial thickness of ZnO film, t_{ZnO} , is much smaller than its width/length and

one-dimensional reactive diffusion equation^[2] in the thickness direction x_3 accounts for the behavior of ZnO hydrolysis. Setting $x_3=0$ at the bottom surface of ZnO film, the water concentration in the ZnO film, w , at time t satisfies the reactive diffusion equation $D \partial^2 w / \partial x_3^2 - kw = \partial w / \partial t$,^[2] where D and k are the diffusivity and reaction constant, respectively. The water concentration is constant at the top surface of the ZnO film $w|_{x_3=t_{ZnO}} = w_0$, and the boundary condition at the bottom of the film is zero water flux $\partial w / \partial x_3|_{x_3=0} = 0$. The above equation can be solved by the method of separation of variables. At the location x_3 and time t , kw water molecules react with ZnO and one water molecule reacts with one ZnO atom. Its integration over the thickness and time gives the mass (per unit area of the cross section) of dissolved ZnO, which in turn gives the remaining thickness of ZnO, \tilde{t}_{ZnO} , normalized by its initial thickness t_{ZnO} as

$$\frac{\tilde{t}_{ZnO}}{t_{ZnO}} \approx 1 - \frac{t}{t_c}, \quad (S1)$$

where

$$t_c = \frac{t_{ZnO}}{\sqrt{kD}} \frac{\rho M_{H_2O}}{w_0 M} \frac{1}{\tanh \sqrt{\frac{kt_{ZnO}^2}{D}}} \quad (S2)$$

is the critical time when the thickness reaches zero, M and M_{H_2O} are the molar masses of ZnO and water, respectively, and ρ is the mass density of ZnO. The diffusivity of water in ZnO sputtered film is independent of pH values and is larger than that in crystalline ZnO.^[3] For diffusivity $D > 2.0 \times 10^{-13}$ cm²/s (and $t_{ZnO}=300$ nm as in experiments and a large range of reaction constant k), the critical time in Eq. (S2) is essentially independent of D . This is because dissolution is dominated by reaction (across the entire thickness) for relatively fast diffusion. The remaining thicknesses given by Eq. (S1) agree well with the experimental measurements for the reaction constants of 3.6×10^{-4} /s, 1.8×10^{-5} /s, 4.7×10^{-6} /s in phosphate buffer solution (PBS, pH 4), DI water (pH 7.5) and bovine serum (pH 8.7), respectively. Eq.

(S2) gives critical time of 1 h, 19 h and 73 h for PBS, DI water and bovine serum solutions, respectively, which agrees reasonably well with experiments in Figure S1a. The dissolution rate is then obtained as

$$v_{dissolution} = -\frac{d\tilde{t}_{ZnO}}{dt} \approx \sqrt{kD} \frac{w_0 M}{\rho M_{H_2O}} \tanh \sqrt{\frac{kt_{ZnO}^2}{D}}. \quad (S3)$$

It gives 313 nm/h, 15.7 nm/h and 4.09 nm/h in PBS, DI water and bovine serum, respectively, consistent with the values reported in the previous experiments.^[4]

2. Piezoelectric analysis of ZnO strips under bending

2.1 Mechanics analysis

For the out-of-plane displacement $w = A[1 + \cos(2\pi x_1/L_{silk})]/2$ shown in Figure 3g for plane-strain analysis ($\varepsilon_{22} = 0$), the bending energy in the silk substrate is related to the curvature w'' by $(\overline{EI}_{silk}/2) \int (w'')^2 ds$, where \overline{EI}_{silk} is the plane-strain bending stiffness of the silk substrate, and the integration is over the length of the silk substrate. The membrane energy can be obtained following the same approach of Song et al.^[5] Minimization of total energy (sum of bending and membrane energies) gives the amplitude A as

$$A = \frac{2}{\pi} \sqrt{L_{silk} \cdot \Delta L - \frac{\pi^2 t_{silk}^2}{3}} \approx \frac{2}{\pi} \sqrt{L_{silk} \cdot \Delta L}, \quad (S4)$$

where t_{silk} is the thickness of the silk substrate, and the last approximation holds when the compression of silk substrate ΔL is much larger than its critical value $\pi^2 t_{silk}^2 / (3L_{silk})$ to initiate buckling. For a 25 μm -thick and 3 cm-long silk substrate, $\pi^2 t_{silk}^2 / (3L_{silk}) \sim 0.07 \mu\text{m}$ is negligible as compared to compression $\Delta L = 1.5 \text{ cm}$ in the experiments.

The bending moment M of the silk substrate is related to the curvature w'' by $M = \overline{EI}_{silk} w''$, where $\overline{EI}_{silk} = (\overline{E}_{silk} t_{silk}^3) / 12$ is the bending stiffness of silk substrate and \overline{E}_{silk} is the plane-strain modulus. For the part of silk substrate covered by the ZnO strips (Figure

S2c), the local curvature is reduced to M/\overline{EI}_{comp} due to the additional bending stiffness of ZnO strips, where $\overline{EI}_{comp} = \sum_{i=1}^n \overline{E}_i t_i \left[t_i^2/3 + \left(\sum_{j=1}^i t_j - y_{neutral} \right) \left(\sum_{j=1}^i t_j - y_{neutral} - t_i \right) \right]$ is the effective bending stiffness of multi-layer structure (Figure S2c) with the silk substrate as the 1st layer ($i=1$) and the summation over all n layers, \overline{E}_i and t_i are the plane-strain modulus and thickness of the i^{th} layer, respectively, and $y_{neutral} = \left[\sum_{i=1}^n \overline{E}_i t_i \left(2 \sum_{j=1}^i t_j - t_i \right) \right] / \left(2 \sum_{i=1}^n \overline{E}_i t_i \right)$ is the distance from the neutral mechanical plane to the bottom of 1st (silk) layer. The membrane strain in ZnO is the axial strain at the mid-plane of ZnO strips, and is given by

$$\varepsilon_m = \left(\overline{EI}_{silk} / \overline{EI}_{comp} \right) w'' h, \quad (S5)$$

where h is the distance between the mid-plane of ZnO strips and the neutral mechanical plane. For the length of ZnO strips much smaller than that of the silk substrate, w'' is evaluated at the center $x_1=0$ of ZnO strips as $w'' = -4\pi \sqrt{\Delta L / L_{silk}} / L_{silk}$. For the structure shown in Figure S2c, $\overline{E}_1 = 3.33 \text{ MPa}$ and $t_1 = 25 \text{ } \mu\text{m}$ for silk, $\overline{E}_2 = 49.1 \text{ MPa}$ and $t_2 = 0.5 \text{ } \mu\text{m}$ for the Mg layer between silk and ZnO strips, $\overline{E}_3 = 157 \text{ MPa}$ and $t_3 = 0.5 \text{ } \mu\text{m}$ for ZnO, and $t_4 = 0.3 \text{ } \mu\text{m}$ for the top Mg layer; these give $\overline{EI}_{silk} / \overline{EI}_{comp} = 0.34$, $y_{neutral} = 20.2 \text{ } \mu\text{m}$ and $h = (t_1 + t_2 + t_3/2) - y_{neutral} = 5.52 \text{ } \mu\text{m}$.

2.2 Piezoelectric analysis

The constitutive model of piezoelectric materials gives the relations among the stress σ_{ij} , strain ε_{ij} , electric field E_i and electric displacement D_i as

$$\begin{Bmatrix} \sigma_{11} \\ \sigma_{22} \\ \sigma_{33} \\ \sigma_{23} \\ \sigma_{31} \\ \sigma_{12} \end{Bmatrix} = \begin{bmatrix} c_{11} & c_{12} & c_{13} & 0 & 0 & 0 \\ c_{12} & c_{11} & c_{13} & 0 & 0 & 0 \\ c_{13} & c_{13} & c_{33} & 0 & 0 & 0 \\ 0 & 0 & 0 & c_{44} & 0 & 0 \\ 0 & 0 & 0 & 0 & c_{44} & 0 \\ 0 & 0 & 0 & 0 & 0 & (c_{11}-c_{12})/2 \end{bmatrix} \begin{Bmatrix} \varepsilon_{11} \\ \varepsilon_{22} \\ \varepsilon_{33} \\ 2\varepsilon_{23} \\ 2\varepsilon_{31} \\ 2\varepsilon_{12} \end{Bmatrix} - \begin{bmatrix} 0 & 0 & e_{31} \\ 0 & 0 & e_{31} \\ 0 & 0 & e_{33} \\ 0 & e_{15} & 0 \\ e_{15} & 0 & 0 \\ 0 & 0 & 0 \end{bmatrix} \begin{Bmatrix} E_1 \\ E_2 \\ E_3 \end{Bmatrix}, \quad (\text{S6})$$

$$\begin{Bmatrix} D_1 \\ D_2 \\ D_3 \end{Bmatrix} = \begin{bmatrix} 0 & 0 & 0 & 0 & e_{15} & 0 \\ 0 & 0 & 0 & e_{15} & 0 & 0 \\ e_{31} & e_{31} & e_{33} & 0 & 0 & 0 \end{bmatrix} \begin{Bmatrix} \varepsilon_{11} \\ \varepsilon_{22} \\ \varepsilon_{33} \\ 2\varepsilon_{23} \\ 2\varepsilon_{31} \\ 2\varepsilon_{12} \end{Bmatrix} + \begin{bmatrix} k_{11} & 0 & 0 \\ 0 & k_{22} & 0 \\ 0 & 0 & k_{33} \end{bmatrix} \begin{Bmatrix} E_1 \\ E_2 \\ E_3 \end{Bmatrix}. \quad (\text{S7})$$

The plane-strain condition $\varepsilon_{22} = 0$ of ZnO strips, together with $\sigma_{33} = 0$ from the traction free on the top surface of the structure, gives $D_3 = \bar{e}\varepsilon_{11} + \bar{k}E_3$, where $\bar{e} = e_{31} - (c_{13}/c_{33})e_{33}$ and $\bar{k} = k_{33} + (e_{33}^2/c_{33})$ are the effective piezoelectric constants. The electric displacement can be further obtained as

$$D_3 = \bar{e}\varepsilon_m + \frac{\bar{k}V}{nt_3} \quad (\text{S8})$$

from the charge equation $dD_3/dx_3 = 0$ and the relation $E_3 = -\partial\phi/\partial x_3$ between the electric field and the electric potential, together with the boundary condition $\phi(x_3 = t_{\text{ZnO}}/2) - \phi(x_3 = -t_{\text{ZnO}}/2) = -V/n$, where V is total voltage between the two ends of the n groups of ZnO strips in series, and t_3 is the thickness of ZnO strips. Eq. (S8) shows that the electric displacement is linear with the membrane strain of ZnO strips, and is independent of the bending strain. Therefore the bending strain does not contribute to the voltage and current output of the MEH given in the following.

2.3 Current

The voltage V across the two ends of the n groups of ZnO strips in series is zero after the ZnO strips are connected to an ampere meter (Figure S2b). The electric displacement in Eq. (S8) then becomes $D_3 = \bar{\epsilon} \epsilon_m$, where ϵ_m is given in Eq. (S5). Its rate gives the current $I = -A_{ZnO} \dot{D}_3$, where $A_{ZnO} = m(w_{ZnO,1}l_{ZnO,1} + w_{ZnO,2}l_{ZnO,2})$ is total area of ZnO strips in each group; $m=10$ is the number of ZnO strips in each group, $w_{ZnO,1}=50\text{ }\mu\text{m}$, $w_{ZnO,2}=90\text{ }\mu\text{m}$, $l_{ZnO,1}=2\text{ mm}$ and $l_{ZnO,2}=90\text{ }\mu\text{m}$ are the widths and lengths of the two rectangular parts of each ZnO strip, respectively (Figure S2a). Substitution of the representative ΔL in the main text into the above formula gives the current, particularly the maximum current in Eq. (1).

2.4 Voltage

For voltage measurement, the voltage V in Eq. (S8) across the two ends of the n groups of ZnO strips in series is no longer zero after the ZnO strips are connected to a voltmeter (Figure S2b). The rate of the displacement in Eq. (S8) gives the current $I = -A_{ZnO} [\bar{\epsilon} \dot{\epsilon}_m + (\bar{k}/nt_3) \dot{V}]$, which, together with the Ohm's law gives Eq. (2) in the main text. Substitution of the representative ΔL in the main text into solution of Eq. (2) gives the voltage, particularly the maximum voltage in Eq. (3).

Figure S3 indicates the intrinsic properties of ZnO thin film by sputtering system. X-ray diffraction (XRD, PhilipsX'pert) patterns shown in Figure S3a were used to assess the orientation and the crystal structure of sputtered ZnO film. Analysis was carried out by performing $2\theta/\omega$ scans, where ω is the angle of incidence relative to the surface and 2θ is the diffraction angle. The diffraction patterns revealed a (001) orientation with an hexagonal structure where the main peak belonging to (002) ZnO is clearly visible. This crystal structure is consistent with that reported.^[6,7] The estimated grain size is $\sim 25\text{ nm}$, estimated

from the width of the XRD peak using the Scherrer formula.^[8] Figure S3b shows scanning electron microscope (SEM) images of a typical ZnO thin film in top and cross-sectional views.

Piezoresponse force microscopy (PFM) studies of ZnO thin films with a Pt bottom electrode were performed using a commercial AFM (Cypher, Asylum Research, USA). Conductive Pt-coated tips (Olympus AC240TM cantilever with a 320 kHz contact resonant frequency, 2N/m spring constant) with a tip radius of 28+/-10 nm were used. A square wave potential was applied to the sample, as shown in Figure 3Sc. The piezoresponse was measured using a superimposed AC bias using the Dual AC Resonance Tracking (DART) PFM technique (see Figure S3d).^[9] The effective piezoelectric coefficient d_{33} of ZnO thin film was found to be 14 pm/V.

2.5 The efficiency calculation of transient ZnO energy harvester

Models of the electromechanics that can determine efficiencies of operation from raw data collected from experiments were developed. In particular, we used these models to calculate i) the mechanical input power required to bend the energy harvester device, ii) the associated electrical output power, and iii) the resulting electromechanical energy conversion efficiency:

The deformation of a silk substrate with the length L_{silk} is defined by classic Euler buckling mechanics. According to post buckling theory,^[10] the external force required to achieve a relative displacement of the two ends of the substrate by ΔL is

$$F(\Delta L) = \left(1 + \frac{\pi}{2} \frac{\Delta L}{L_{silk}}\right) \frac{4\pi^2 \overline{EI}_{silk}}{L_{silk}^2}$$

where $\overline{EI}_{silk} = \overline{E}_{silk} w_{silk} t_{silk}^3 / 12$ is the bending stiffness, and \overline{E}_{silk} , w_{silk} and t_{silk} are the effective Young's modulus, the width and the thickness of the substrate, respectively. The work associated with bending from the flat state to the state of maximum curvature is given by

$$W = \int_0^{\Delta L_{\max}} F(\Delta L) d\Delta L = \frac{\pi^2 \bar{E}_{\text{silk}} \Delta L_{\max} w_{\text{silk}} t_{\text{silk}}^3}{3L_{\text{silk}}^2} \left(1 + \frac{\pi}{4} \frac{\Delta L_{\max}}{L_{\text{silk}}} \right)$$

For the structure shown in Figure S2d, $\bar{E}_{\text{silk}} = 3.33 \text{ Mpa}$, $L_{\text{silk}} = 3 \text{ cm}$, $\Delta L_{\max} = 1.5 \text{ cm}$, $t_{\text{silk}} = 25 \mu\text{m}$ and $w_{\text{silk}} = 2 \text{ cm}$, the work (i.e. the input energy) is 79.49nJ.

i) The input power is simply given by this quantity divided by the time for this deformation (T=2.3 s for experiments reported here)

$$P_{\text{in}} = \frac{W_{\text{in}}}{T} = \frac{79.49 \text{ nJ}}{2.3 \text{ s}} = 34.55 \text{ nW}$$

ii) The electrical energy output by bending the energy harvester device is calculated by integrating the ratio of the square of the voltage and the resistance over time by following formula ^[11]

$$W_{\text{out}} = \int_0^T V^2 / R dt$$

where V and $R = 2.3 \times 10^9 \Omega$ are the measured output voltage and the resistance of the voltmeter, respectively.

Thus,

$$P_{\text{out}} = \frac{W_{\text{out}}}{T} = 0.097 \text{ nW}$$

iii) The electromechanical energy conversion efficiency of the transient, ZnO energy harvester on a thin film silk substrate can be calculated as the ratio between generated electrical energy and the mechanical input power required to bend the energy harvester device.

$$\frac{P_{\text{out}}}{P_{\text{in}}} = \frac{0.097 \text{ nW}}{34.55 \text{ nW}} \times 100 = 0.28\%$$

References

- [1] C. David, J. Galceran, C. Rey-Castro, J. Puy, E. Companys, J. Salvador, J. Monne, R. Wallace, A. Vakourov, *J. Phys. Chem.* **2012**, *116*, 11758.
- [2] P. V. Danckwerts, *Transactions of the Faraday Society* **1950**, *46*, 300.
- [3] W. J. Moore, E. L. William, *Discussions of the Faraday Society* **1959**, *28*, 86.
- [4] H. Gerischer, N. Sorg, *Electrochimica Acta.* **1992**, *37*, 827.
- [5] J. Song, Y. Huang, J. Xiao, S. Wang, K. C. Hwang, H. C. Ko, D. H. Kim, M. P. Stoykovich, J. A. Rogers, *Journal of Applied Physics* **2009**, *105*, 123516.
- [6] N. H. Al-Hardan, M. J. Abdullah, A. A. Aziz, H. Ahmad, M. Rashid, *Physica B* **2010**, *405*, 1081.
- [7] R. Ondo-Ndong, G. Ferblantier, F. Pascal-Delannoy, A. Boyer, A. Foucaran, *Microelectronics Journal* **2003**, *34*, 1087.
- [8] S. Ilican, Y. Caglar, M. Caglar, *Journal of Optoelectronics and Advance Materials* **2008**, *10*, 2578.
- [9] B. J. Rodriguez, C. Callahan, S. Kalinin, R. Proksch, *Nanotechnology* **2007**, *18*, 475-504.
- [10] Y. Su, J. Wu, Z. Fan, K. C. Hwang, J. Song, Y. Huang, J. A. Rogers, *Journal of the Mechanics and Physics of Solids* **2012**, *60*, 487.
- [11] R. Andosca, T. Gus McDonald, V. Genova, S. Rosenberg, J. Keating, C. Benedixen, J. Wu, *Sensors and Actuators A* **2012**, *178*, 76.

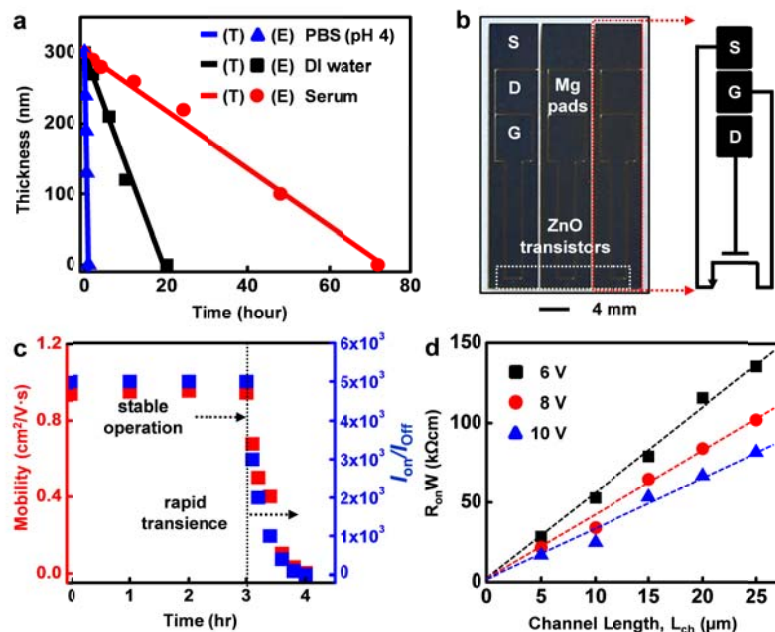


Figure S1. a) Experimental (E) and theoretical (T) changes in the thickness of a thin film of ZnO as a function of time, during dissolution in different solutions: phosphate buffer solution (PBS, pH 4, blue), DI water (pH 7.5, black), bovine serum (pH 8.7, red). b) Image of the ZnO TFT used to study dissolution kinetics at the device level, with a circuit diagram. c) Calculated mobility (red) and on/off ratio (blue), corresponding to transfer curves in the right frame of Figure 2c. d) Width-normalized on-state resistance at various channel lengths and gate biases.

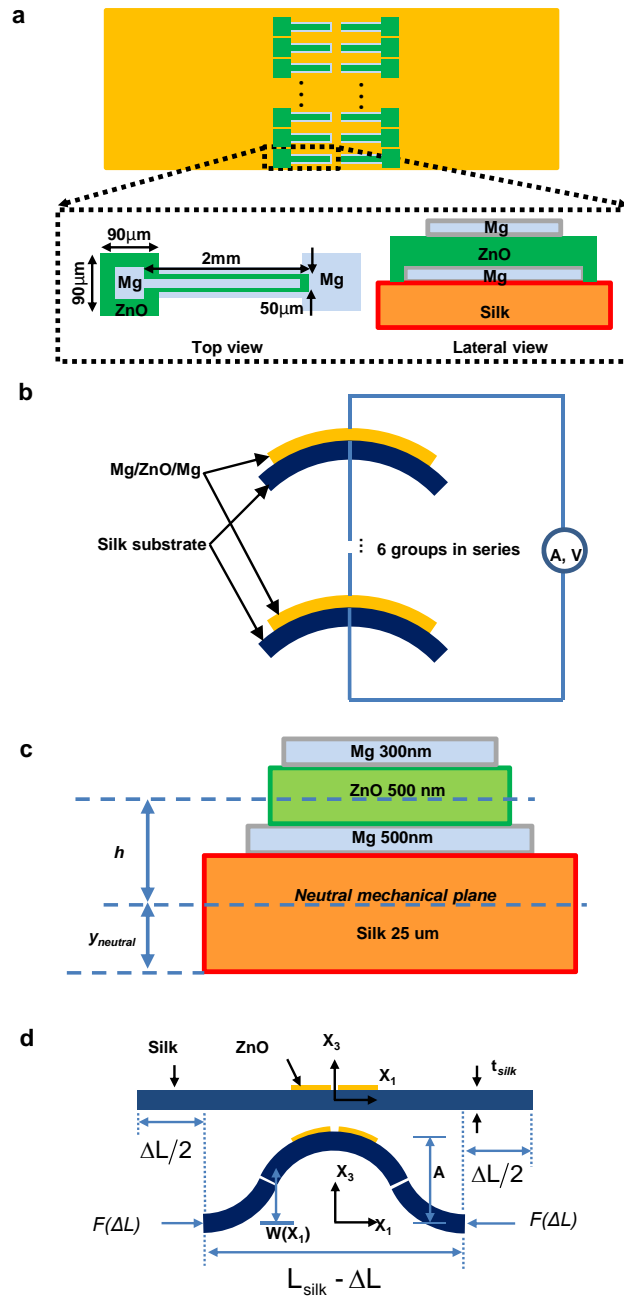


Figure S2. a) Schematic illustration of an array of ZnO strips, and top and lateral views of a single strip. b) Schematic illustration of a buckled array of ZnO strips on a silk substrate. c) Schematic description of the membrane strain in the various layers of a ZnO MEH and the position of the neutral mechanical plane of the device. d) Schematic illustration of the theoretical shape for buckling of a device under compression.

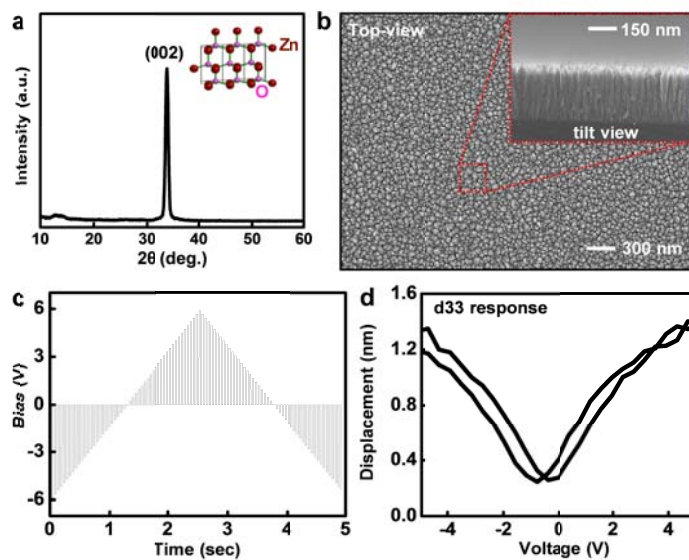


Figure S3. a) X-ray diffraction pattern of a thin film of ZnO, with preferred orientation labeled (002). b) Top view scanning electron microscope (SEM) image of a sputtered ZnO thin film, with cross sectional image in the inset. c) Typical bias profile for d_{33} measurement. (Details in SI). d) Measured displacements as a function of voltage applied to the ZnO thin film.